Research Article | Vol. 31, No. 16 / 31 Jul 2023 / Optics Express 27006
Optics EXPRESS

Topological photonic crystal fiber with honeycomb structure

HONG HUANG,[1,2] ZHI-YAO NING,[1,2] TOSHIKAZE KARIYADO,[2] TOMOHIRO AMEMIYA,[3] AND XIAO HU[1,2,*]

[1]Research Center for Materials Nanoarchitectonics (MANA), National Institute for Materials Science (NIMS), Tsukuba 305-0044, Japan
[2]Graduate School of Science and Technology, University of Tsukuba, Tsukuba 305-8571, Japan
[3]Institute of Innovative Research, Tokyo Institute of Technology, Tokyo 152-8552, Japan
*HU.Xiao@nims.go.jp

Abstract: We analyze a new type of photonic crystal fiber which consists of the core and cladding that distinct in topology by tuning the position of air holes in each hexagonal unit cell where the C_{6v} symmetry is respected. The *p*-*d* band inversion between the core and cladding leads to topological interface modes inside the band gap, which can propagate along the fiber with a nonzero momentum in perpendicular to the corss section of a fiber. The helical topological interface modes possess the pseudospin-momentum locking effect inherited from the corresonding two-dimensional photonic crystal characterized by the Z_2 topology. The wave functions for the topological interface modes are analytically studied and compared successfully to the numerical results, enlighting a novel way to use photonic crystal fiber to transfer information.

1. Introduction

The optical fiber system gives high data rate, low signal loss and cheap cost comparing with other communication media such as copper wire-based systems, playing a vital role in the information age [1–3]. In conventional optical fibers, a core with higher refractive index is covered by cladding with lower refractive index. Because of total internal reflection, light waves can propagate in optical fibers with low loss. The number of guided modes propagating inside optical fibers depends on the diameter of the core, which enables us to make single-mode fibers, few-mode fibers and multi-mode fibers [4,5]. Besides being used for communication, optical fibers are also widely used as fiber lasers and fiber-optic sensors [6–9].

Another possible architecture is a photonic crystal fiber (PCF), which is based on the properties of photonic crystals (PhCs) [10–13]. There are two major types of PCFs: solid core PCFs and hollow core PCFs. The former one has a solid core surrounded by cladding with a periodic array of holes of air (or materials with lower refractive index), where light is confined with the mechanism similar to the conventional optical fibers, i.e., air holes reduce the effective refractive index in the cladding region, resulting in refractive index difference between the core and cladding made of the same material. On the other hand, in the hollow core PCF, the solid core is replaced by a large air hole while keeping the air hole array in the cladding. Then a different mechanism for the light confinement is at work. The PhC in the cladding is designed to have a photonic band gap, which prevents light in the hollow core from penetrating into the cladding provided the frequency of the light is in the frequency range of the band gap. The virtue of the latter structure is that the guided light waves are hardly affected by the bending of fibers, since it does not rely on the total internal reflection.

The concept of topology can be introduced to construct new PCFs. Topological states of matter have been the subject of intense research in recent years [14–17]. Topologically nontrivial states are featured by protected edge/interface states, which appear at the boundary between two regions with different topological invariants, and provide robust propagating modes that are

#496046 https://doi.org/10.1364/OE.496046
Journal © 2023 Received 26 May 2023; revised 12 Jul 2023; accepted 17 Jul 2023; published 28 Jul 2023

Optics EXPRESS

immune to impurity scattering. In 2008, Haldane and Raghu proposed a photonic counterpart of the quantum Hall effect [18,19]. Because topological states in photonic systems can be achieved at the room temperature, it inspires lots of studies and topological PhCs form an established subfield of the PhC study now [20–22]. These studies give a new idea for constructing PCFs based on the concept of topology. For instance, recent proposals include topological one-way fiber of second Chern number in a three-dimensional magnetic Weyl PhC [23], PCFs using the topological end states [24,25], and topological PCFs using the valley-Hall effect [26–28].

In the two-dimensional (2D) PhC with honeycomb structure [22], it is proposed that, the nontrivial topology can be easily achieved by tuning the lattice constant while keeping the distance between dielectric cylinders inside each hexagonal unit cell unchanged, or keeping the lattice constant while tuning the internal coordinates of cylinders in the unit cell (see also [29,30]). A pseudospin defined by orbital angular momentum in a unit cell gonverns the direction of propagation of the topological interface modes, suggesting a method to control the direction of propagating light waves. This scheme has already been realized experimentally and extended to several systems [31–35] and it is found to be useful to construct topological PhCs with confined modes carring opposite pseudospin. However, interface modes discussed and experimetally realized so far are limited in two dimensions, with zero out-of-plane momentum k_z. In order to use these modes for constructing PCFs, it is important to investigate the properties of topological interface modes with a nonzero out-of-plane momentum k_z in a three-dimensional space.

2. Photonic crystals uniform in out-of-plane direction

In this paper, we study a PhC that has hexagonal unit cells that contain six equilateral triangular air holes in the xy plane as shown in Fig. 1 [22,34] and uniform along the z direction. We fix the lattice constant a_0 of PhC in our PhC structure and L the side length of each equilateral triangle in a unit cell, while tuning the distance R between center of the unit cell and the center of air holes to control the photonics topology.

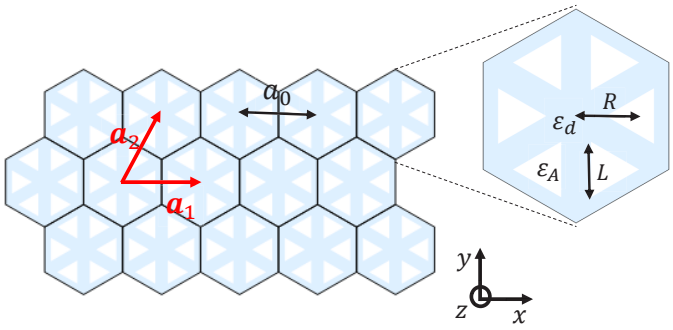

Fig. 1. Photonic crystal with hexagonal unit cells, which is periodic in the xy plane but uniform along the z direction. $\boldsymbol{a}_1$ and $\boldsymbol{a}_2$ are lattice vectors and the lattice constant is a_0. Each unit cell contains six equilateral triangular air holes with side length L. These air holes are away from the center of unit cell with a distance R. ε_d and ε_A are dielectric constant for dielectric and air respectively.

We consider a harmonic mode of frquency ω with electric and magnetic fields in the form [36]

$$\boldsymbol{E}(\boldsymbol{r}, z, t) = \boldsymbol{E}(\boldsymbol{r}, z)e^{-\mathrm{i}\omega t} \tag{1}$$

and

$$\boldsymbol{H}(\boldsymbol{r}, z, t) = \boldsymbol{H}(\boldsymbol{r}, z)e^{-\mathrm{i}\omega t} \tag{2}$$

Optics EXPRESS

respectively, where $\boldsymbol{r}$ is a 2D position vector. These harmonic modes in the PhC satisfy the Maxwell equations:

$$\nabla \times \boldsymbol{E}(\boldsymbol{r}, z) = \mathrm{i}\omega\mu\mu_0 \boldsymbol{H}(\boldsymbol{r}, z), \tag{3a}$$

$$\nabla \times \boldsymbol{H}(\boldsymbol{r}, z) = -\mathrm{i}\omega\varepsilon(\boldsymbol{r})\varepsilon_0 \boldsymbol{E}(\boldsymbol{r}, z), \tag{3b}$$

$$\nabla \cdot \varepsilon(\boldsymbol{r})\varepsilon_0 \boldsymbol{E}(\boldsymbol{r}, z) = 0, \tag{3c}$$

$$\nabla \cdot \boldsymbol{H}(\boldsymbol{r}, z) = 0, \tag{3d}$$

where μ_0, ε_0, μ, and $\varepsilon(\boldsymbol{r})$ are the vacuum magnetic permeability, the vacuum dielectric constant, relative permeability, and relative dielectric constant, respectively. We assume μ to be unity without position dependence throughout the paper. On the other hand, $\varepsilon(\boldsymbol{r})$ has position dependence: ε_d at the dielectric and ε_A at the air holes. Reflecting our structure, $\varepsilon(\boldsymbol{r})$ only depends on x and y without z dependence.

For fibers with air holes arranged in honeycomb lattice, TE-like modes with dominant in-plane electric field in the PhC are available. Because $\varepsilon(\boldsymbol{r})$ is independent of z, the dominant in-plane components of electric field takes the form

$$\boldsymbol{E}(\boldsymbol{r}, z) = [\boldsymbol{e}_x E_x(x, y) + \boldsymbol{e}_y E_y(x, y)]Z(z), \tag{4}$$

where $\boldsymbol{e}_x$/$\boldsymbol{e}_y$ is the unit vector in x/y direction. For simplicity, we neglect the small E_z component in the following analytic derivation.

From the Maxwell Eqs. (3), we can derive the following master equation for $\boldsymbol{E}(\boldsymbol{r})$

$$\frac{1}{\varepsilon(\boldsymbol{r})}\nabla \times \nabla \times \boldsymbol{E}(\boldsymbol{r}) = \frac{\omega^2}{c^2}\boldsymbol{E}(\boldsymbol{r}), \tag{5}$$

where $c = 1/\sqrt{\mu_0\varepsilon_0}$ is the speed of light in cacuum. Substituting Eq. (4) into the master Eq. (5), we can separate $Z(z)$ as

$$\frac{d^2 Z}{dz^2} + k_z^2 Z = 0, \tag{6}$$

and the solution $Z(z) = e^{\mathrm{i}k_z z}$ travels in the positive z direction. The xy-dependent part of these modes are $E_x(x, y)$ and $E_y(x, y)$, which satisfy

$$\frac{1}{\varepsilon(\boldsymbol{r})}\frac{\partial}{\partial y}\left(\frac{\partial E_y}{\partial x} - \frac{\partial E_x}{\partial y}\right) + \left(\frac{k_z^2}{\varepsilon(\boldsymbol{r})} - \frac{\omega^2}{c^2}\right)E_x = 0, \tag{7a}$$

$$\frac{1}{\varepsilon(\boldsymbol{r})}\frac{\partial}{\partial x}\left(\frac{\partial E_x}{\partial y} - \frac{\partial E_y}{\partial x}\right) + \left(\frac{k_z^2}{\varepsilon(\boldsymbol{r})} - \frac{\omega^2}{c^2}\right)E_y = 0. \tag{7b}$$

It can be derived from Eq. (3a) that the in-plane magnetic field H_x is proportional to $\partial_z E_y = \mathrm{i}k_z E_y$ and H_y is proportional to $\partial_z E_x = \mathrm{i}k_z E_x$. Therefore, for $k_z = 0$, only the z component of magnetic field $\boldsymbol{H}(\boldsymbol{r}, z)$ is nonzero, and the modes propagate inside the xy plane. On the contrary, here we need to consider modes that can propagate along the z direction, which means $k_z \neq 0$. In this case, the magnetic field $\boldsymbol{H}(\boldsymbol{r}, z)$ has three nonzero components.

We can numerically calculate the frequency band structure of the PhC described in Fig. 1 using COMSOL [37]. In our calculation, $\varepsilon_d = 11.7$, $\varepsilon_A = 1$, $a_0 = 0.8\mu m$, and $L = 0.3a_0$ are used, unless otherwise specified. These parameters are taken from previous experimental works on silicon-based topological PhC. As will be shown later, the center of topological bandgap and bandgap are 152 THz and 7 THz, with targeting wavelength close the telecommunication band when the finite out-of-plane momentum is taken into account. Therefore, the present work provides a basic guideline for designing practical topological PCFs.

Optics EXPRESS

For $R = 0.93a_0/3$, a band gap opens with $k_z = 0$ as shown in Fig. 2(a), where d modes are above the band gap and p modes are below the band gap with d and p modes shown in Fig. 2(c). The frequency band structure for $k_z = 0.1 \times 2\pi/a_0$ is shown in Fig. 2(b). Even though a nonzero k_z is considered here and all three components of the mangetic field are finite, we find that the z component of the magnetic field can still be classified as p or d modes around the band gap at the Γ point with distribution of d and p modes very similar to those for $k_z = 0$. It is found that the nonzero k_z shifts slightly the frequency band structure to a higher frequency.

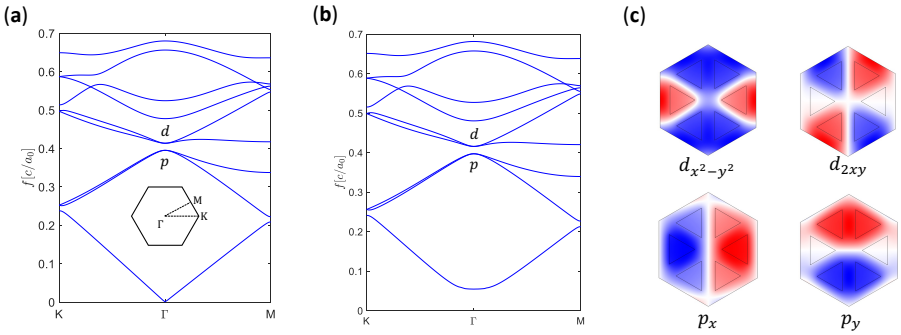

Fig. 2. (a) Frequency band structure for $R = 0.93a_0/3$ and $k_z = 0$. A band gap from $0.3953c/a_0$ to $0.4137c/a_0$ opens with d modes above the band gap and p modes below the band gap. (b) Frequency band structure for $R = 0.93a_0/3$ and $k_z = 0.1 \times 2\pi/a_0$, where the band gap is from $0.3970c/a_0$ to $0.4156c/a_0$. (c) The z component of magnetic field H_z of d and p modes for $k_z = 0.1 \times 2\pi/a_0$. $\varepsilon_d = 11.7$, $\varepsilon_A = 1$, $a_0 = 0.8\mu m$, and $L = 0.3a_0$ are used in all calculations, unless otherwise specified.

On the contrary, for $R = 1.05a_0/3$, the d modes are below the band gap and the p modes are above the band gap as shown in Figs. 3(a) and 3(b) for $k_z = 0$ and $k_z = 0.1 \times 2\pi/a_0$ respectively. For $k_z = 0$, the band gaps in Figs. 2(a) and 3(a) overlap with each other, while the band gaps in Figs. 2(b) and 3(b) overlap with each other for $k_z = 0.1 \times 2\pi/a_0$. Even R is different for the two structures, the degenerate p and d modes exhibit basically the same distributions, as seen in Figs. 2(c) and 3(c). As in the case of $k_z = 0$, this p-d band inversion for nonzero k_z indicates the PhC with $R > a_0/3$ is topologically distinct from that with $R < a_0/3$ [22].

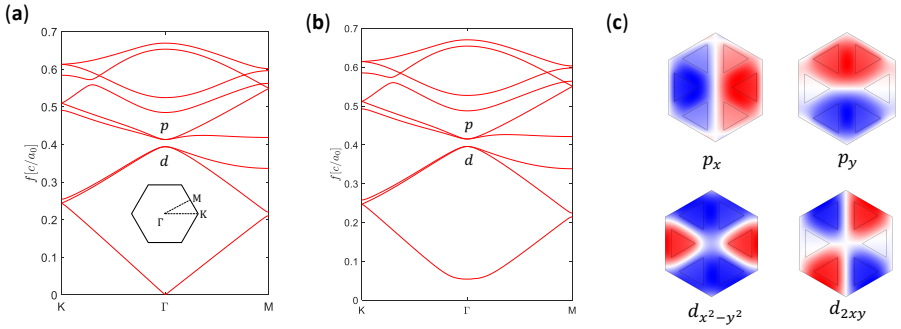

Fig. 3. (a) Frequency band structure for $R = 1.05a_0/3$ and $k_z = 0$. A band gap from $0.3943c/a_0$ to $0.4133c/a_0$ opens with p modes above the band gap and d modes below the band gap. (b) Frequency band structure for $R = 1.05a_0/3$ and $k_z = 0.1 \times 2\pi/a_0$, where the band gap is from $0.3960c/a_0$ to $0.4152c/a_0$. (c) The z component of magnetic field H_z of p and d modes for $k_z = 0.1 \times 2\pi/a_0$.

Optics EXPRESS

The p and d modes shown in Figs. 2(c) and 3(c) can be recombined into $p_\pm$ and $d_\pm$, where $p_\pm = p_x \pm \mathrm{i}p_y$ and $d_\pm = d_{x^2+y^2} \pm \mathrm{i}d_{2xy}$. As shown in Fig. 4, states $p_\pm \sim e^{\pm \mathrm{i}\theta}$ and $d_\pm \sim e^{\pm \mathrm{i}2\theta}$ with azimuthal θ measured from the positive x-axis shown Fig. 1 carry quasi orbital angular momentum (OAM) ± 1 and ± 2 respectively, indicated by 2π and 4π phase windings in $\arg(H_z)$. The modes p_+ and d_+ form the pseudospin-up sector, while p_- and d_- form the pseudospin-down sector.

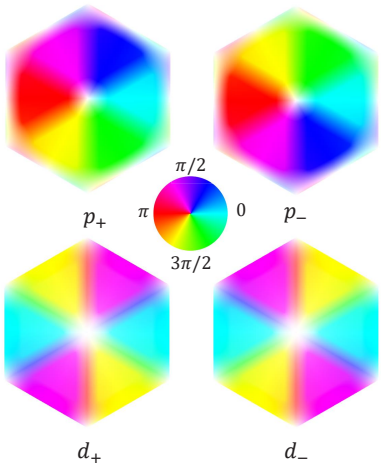

Fig. 4. Phase of H_z, $\arg(H_z)$, for $p_\pm$ and $d_\pm$ with azimuthal θ measured from the positive x-axis shown in Fig. 1. The modes $p_\pm$ and $d_\pm$ carry quasi orbital angular momentum (OAM) ± 1 and ± 2 respectively, presenting as 2π and 4π phase winding in $\arg(H_z)$ in the hexagonal unit cell. The modes p_+ and d_+ (p_- and d_-) form the pseudospin-up (pseudospin-down) sector.

For $k_z = 0$, p_+ (d_+) and p_- (d_-) are related by the time-reversal symmetry $\mathcal{T}$. This relation is broken in the case $k_z \neq 0$, where the time-reversal partner for p_+ with $e^{\mathrm{i}k_z z}$ is p_- with $e^{-\mathrm{i}k_z z}$. We can see that the master Eq. (5) also satisfies the mirror symmetry $\mathcal{M}$ with respect to the xy plane, which changes k_z to $-k_z$ in addition to the time-reversal symmetry. Reflecting the fact that both $e^{\mathrm{i}k_z z}$ and $e^{-\mathrm{i}k_z z}$ are solutions of Eq. (6), p_- with $e^{\mathrm{i}k_z z}$ and $e^{-\mathrm{i}k_z z}$ are different only in the direction of propagation in the z component. Therefore, in the case $k_z \neq 0$, p_+ (d_+) and p_- (d_-) with $e^{\mathrm{i}k_z z}$ are still degenerate and related by symmetry $\mathcal{TM}$.

In Figs. 5(a) and 5(b), we show the frequency dispersions up to larger k_z for the modes at the band edges where a parabolic shape is clearly observed, which is consistent with Eq. (7) taking the dielectric constant as an averaged one. As can be seen in Eq. (7), the wavefunctions are separable into the direction of fiber axis and the transverse directions with the former described by a plane wave, and the parabolic dispersions in Figs. 5(a) and 5(b) corresponds to a group velocity proportional to k_z along the fiber axis. Therefore, it is clear that the photonics topology induced by the band inversion of $p - d$ modes at Γ point of the BZ in the transverse directions remains essentially the same as that addressed in 2D systems, and the ring-cavity modes in 2D case can be transplanted to fiber systems. Specifically, the ring-cavity modes with global OAM and pseudospin are similar to the pure 2D case studied in Refs. [38] and [39] in the transverse directions. In what follows, to be comprehensive, we reformulate the physics in the transverse directions and proceed to analyze in detail the wavefunctions.

Optics EXPRESS

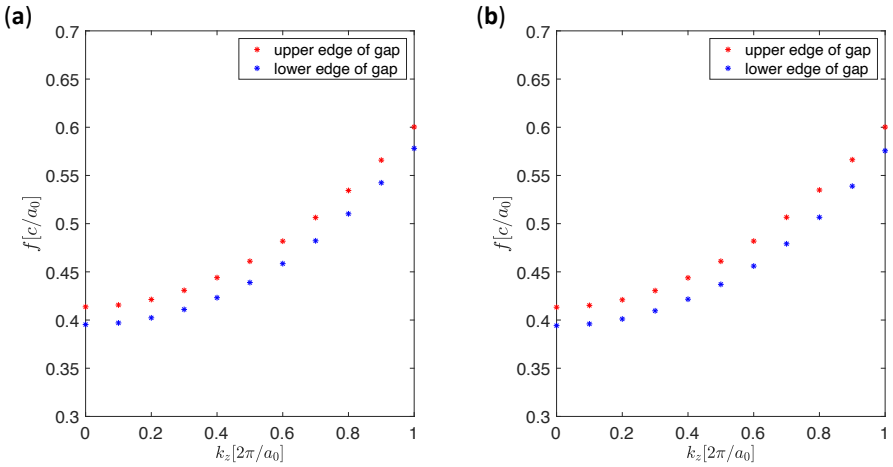

Fig. 5. (a) Dispersion relation referring to the band edges at the Γ point in the transverse directions for $R = 0.93a_0/3$. (b) Same as (a) but for $R = 1.05a_0/3$. The parabolic dispersions give the group velocity proportional to k_z along the z axis.

3. Topological interface modes carrying finite out-of-plane momentum

Now we consider a PCF whose cross-section is shown schematically in Fig. 6(a), where a topological PhC with the parameters used in Fig. 3(a) is surrounded by a trivial PhC with the parameters used in Fig. 2(a). With finite out-of-plane momentum, there will be several topological interface modes, travelling along the PCF with opposite rotation direction depending on pseudospin, as shown in the schematic diagram Fig. 6(b).

For the sake of simplicity, we use a hexagonal shape of fiber with hexagonal core in our calculation, where the side length of the core is $12a_0$ and the side length of the fiber is $18a_0$. Inside the overlapped band gap, there are couples of interface modes confined at the interface between the topological and trivial regions in real space, as shown in Fig. 7, where two interface modes are picked to show the field strength $|H_z|^2$.

The confined interface modes can be captured by the $\boldsymbol{k}\cdot\boldsymbol{p}$ Hamiltonian with the basis set $[p_+\ d_+\ p_-\ d_-]$ [22,38]:

$$H_{\boldsymbol{k}} = \begin{bmatrix} M + B\hat{k}^2 & A\hat{k}_+ & C\hat{k}_-^2 & 0 \\ A^*\hat{k}_- & -M - B\hat{k}^2 & 0 & C\hat{k}_+^2 \\ C\hat{k}_+^2 & 0 & M + B\hat{k}^2 & A\hat{k}_- \\ 0 & C\hat{k}_-^2 & A^*\hat{k}_+ & -M - B\hat{k}^2 \end{bmatrix}, \tag{8}$$

where $\hat{k}_\pm = \hat{k}_x \pm \mathrm{i}\hat{k}_y$ and $\hat{k}^2 = \hat{k}_x^2 + \hat{k}_y^2$, which describes the band dispersion near the band gap. Since the Dirac mass term M determines the topology in this model, the topological PCFs can be treated by considering the position dependence of M [40,41]. In Eq. (8), the off-diagonal block

$$H_{\mathrm{CP}} = \begin{bmatrix} C\hat{k}_-^2 & 0 \\ 0 & C\hat{k}_+^2 \end{bmatrix} \tag{9}$$

connects the pseudospin-up and -down sectors. By neglecting this term, the diagonal blocks corresponding to the opposite pseudospins are decoupled, and we can consider these block separately [33].

Optics EXPRESS

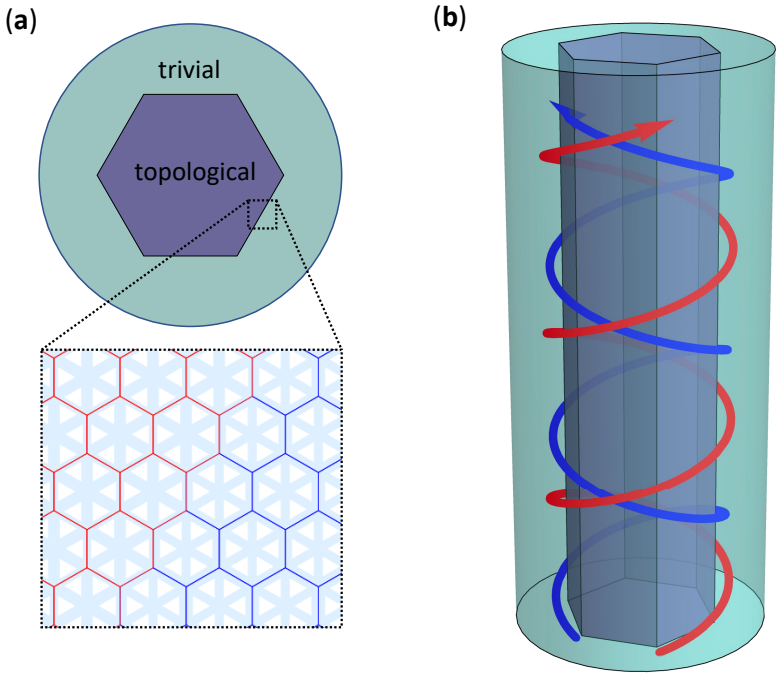

Fig. 6. (a) Cross-section of photonic crystal fiber (PCF), where a topological photonic crystal forms the core surrounded by a trivial photonic crystal as the cladding. (b) Schematic diagram of topological interface modes in PCF, where propogation direction depends on pseudospin.

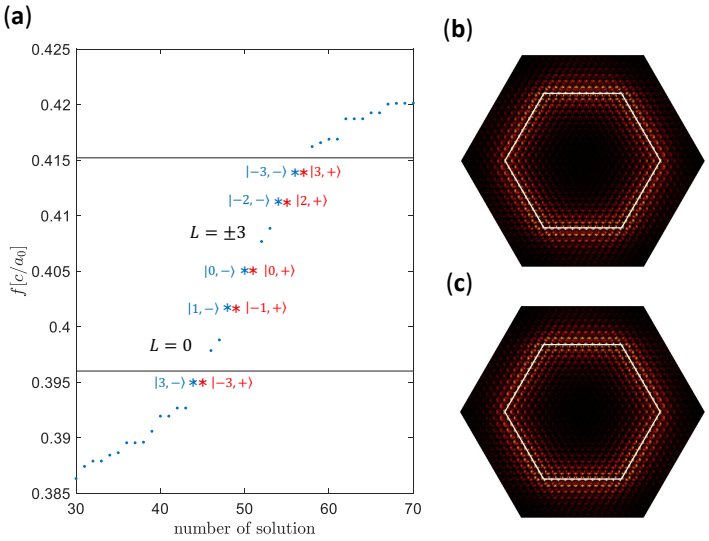

Fig. 7. (a) Spectrum of the PCF structure in Fig. 6(a) calculated by COMSOL. There are several pairs of interface modes $|l,\pm\rangle$ related to each other by symmetry $\mathcal{TM}$. The band edges around the Γ point of Fig. 3(b) for bulk systems are denoted by black lines. (b)-(c) $|H_z|^2$ of interface modes $|0,+\rangle$ and $|0,-\rangle$ respectively, where topological photonic crystal is inside the white lines.

Optics EXPRESS

In order to analyze the $\boldsymbol{k}\cdot\boldsymbol{p}$ Hamiltonian for a topological PCF with the cross-section shown in Fig. 6(a), it is convenient to consider the polar coordinate

$$\hat{k}_x = \cos\phi\hat{k}_r - \sin\phi\hat{k}_\phi, \tag{10a}$$

$$\hat{k}_y = \sin\phi\hat{k}_r + \cos\phi\hat{k}_\phi, \tag{10b}$$

where the position of unit cell center is given by $\boldsymbol{r} = (r, \phi)$ with r the distance measured from the center of fiber and ϕ the associated azimuthal angle measured from the positive x-axis shown in Fig. 1. In the polar coordinate, $\hat{k}_r = -\mathrm{i}\partial_r$ and $\hat{k}_\phi = (1/r)(-\mathrm{i}\partial_\phi)$, and

$$\hat{k}_\pm = \mathrm{e}^{\pm\mathrm{i}\phi}[-\mathrm{i}\partial_r \pm \mathrm{i}(1/r)(-\mathrm{i}\partial_\phi)]. \tag{11}$$

The block corresponding to pseudospin up, i.e., the 2×2 block spanned by $[p_+\ d_+]$, can be written as $H_+ = H'_+ + H''_+$ [38,39], where

$$H'_+ = \begin{bmatrix} M & A\mathrm{e}^{\mathrm{i}\phi}\hat{k}_r \\ A^*\mathrm{e}^{-\mathrm{i}\phi}\hat{k}_r & -M \end{bmatrix}, \quad H_+ = \begin{bmatrix} B(\hat{k}_r^2 + \hat{k}_\phi^2 - \frac{1}{r}\partial_r) & \mathrm{i}A\mathrm{e}^{\mathrm{i}\phi}\hat{k}_\phi \\ -\mathrm{i}A^*\mathrm{e}^{-\mathrm{i}\phi}\hat{k}_\phi & B(\hat{k}_r^2 + \hat{k}_\phi^2 - \frac{1}{r}\partial_r) \end{bmatrix}. \tag{12}$$

We derive the eigenvalue by treating H'_+ as the unperturbed Hamiltonian, and H''_+ as the perturbation. At the interface between the topological region ($M>0$) and trivial region ($M<0$), H'_+ hosts the zero-energy eigenstate [38,39]

$$|+\rangle = \frac{1}{\sqrt{2}}[p_+\ d_+]\begin{bmatrix} \mathrm{e}^{\mathrm{i}\phi} \\ 1 \end{bmatrix} F(r), \tag{13}$$

where $F(r)$ is the r-dependent Jackiw-Rebbi soliton solution. (As the zeroth order approximation, ϕ dependence of M is neglected.) [42] In the state $|+\rangle$, the perturbation Hamiltonian H_+ can be written as [38,39]

$$\begin{aligned}
&\langle +|H_+|+\rangle \\
&= \frac{1}{2}\int_0^\infty dr \begin{bmatrix} \mathrm{e}^{-\mathrm{i}\phi} & 1 \end{bmatrix} F(r) \begin{bmatrix} B(\hat{k}_r^2 + \hat{k}_\phi^2 - \frac{1}{r}\partial_r) & \mathrm{i}A\mathrm{e}^{\mathrm{i}\phi}\hat{k}_\phi \\ -\mathrm{i}A^*\mathrm{e}^{-\mathrm{i}\phi}\hat{k}_\phi & -B(\hat{k}_r^2 + \hat{k}_\phi^2 - \frac{1}{r}\partial_r) \end{bmatrix} \begin{bmatrix} \mathrm{e}^{\mathrm{i}\phi} \\ 1 \end{bmatrix} F(r) \\
&\approx \frac{1}{2}\Big(\int_0^\infty dr|A|F(r)^2\Big)[\hat{k}_\phi + \mathrm{e}^{-\mathrm{i}\phi}\hat{k}_\phi\mathrm{e}^{\mathrm{i}\phi}] \\
&= \frac{1}{2r_0}\Big(\int_0^\infty dr|A|F(r)^2\Big)[-2\mathrm{i}\partial_\phi + 1] = \hbar\omega_0[-2\mathrm{i}\partial_\phi + 1],
\end{aligned} \tag{14}$$

where $\hbar\omega_0 = (\int_0^\infty dr|A|(r)F(r)^2)/2r_0$ is a small value for a system with large radius and we neglect $\hat{k}_\phi^2$ since it is much smaller than $\hat{k}_r^2$ and $\frac{1}{r}\partial_r$ at the interface. Therefore, the eigenvalue equation of H_+ in the basis $|+\rangle$ is

$$\hbar\omega_0[-2\mathrm{i}\partial_\phi + 1]\psi(\phi) = \hbar\omega\psi(\phi). \tag{15}$$

It is clear that the eigen solutions is given by $\psi_l(\phi) = \mathrm{e}^{\mathrm{i}l\phi}$ with corresponding eigenvalues $\omega_l = (2l+1)\omega_0$. Therefore, the eigenstates of H_+ are [38,39]

$$|l,+\rangle = \frac{\mathrm{e}^{\mathrm{i}l\phi}}{\sqrt{2}}[p_+\ d_+]\begin{bmatrix} \mathrm{e}^{\mathrm{i}\phi} \\ 1 \end{bmatrix} F(r) \tag{16}$$

with eigenenergy(eigenfrequency) proportional to $2l+1$, where l is an integer referring to the global OAM of the cavity. Similarly, for the pseudospin-down block spanned by $[p_-\ d_-]$, the

Optics EXPRESS

topological interface modes are given by

$$|-l,-\rangle = \frac{e^{-il\phi}}{\sqrt{2}}\,[p_-\ d_-]\begin{bmatrix} e^{-i\phi} \\ 1 \end{bmatrix} F(r). \tag{17}$$

In addition to the global OAM, the modes p_+ (d_+) provides local OAM of 1 (2). Therefore, the total OAM L of $|l,+\rangle$ is $L = l + 2$ including the $e^{i\phi}$ term in Eq. (13). Note that the nondegenerate modes inside the band gap correspond to $L = 0$ and $L = \pm 3$ in Fig. 7(a), which can be explained by coupling matrix (9) [38]. Since the fiber conserves inversion symmetry with respect to the center of the xy plane, the states with odd (even) L have odd (even) parity with respect to the inversion symmetry about the fiber center.

The phase of H_z for mode $|0,+\rangle$ is shown in Fig. 8(a), where the counterclockwise evolution of phase inside of the unit cells indicates an up pseudospin. To check the phase distribution in mode $|0,+\rangle$, we show close up views of the several parts in the outermost layer of topological hexagonal unit cells in Fig. 8(b). Starting with the hexagon 1, we look at the section indicated by the triangle. The change of color is observed during the rotation of the section with respect to the fiber center. Its color changes from magenta to yellow as it rotates from the hexagon 1 to the hexagon 2. In the hexagon 2, we look at the section denoted by the triangle since it acquires $\pi/3$ phase in the rotation. As the section goes through a 2π rotation from the hexagon 1 to the hexagon 6, we can see that the color changes by two loops in the counterclockwise order of the color disk, as presented in the color change of arrows. Namely, we observe a 4π change of phase when one goes a round along the azimuthal angle couterclockwise consistent with a total OAM $L = 2$, corresponding to $l = 0$ with pseudospin up.

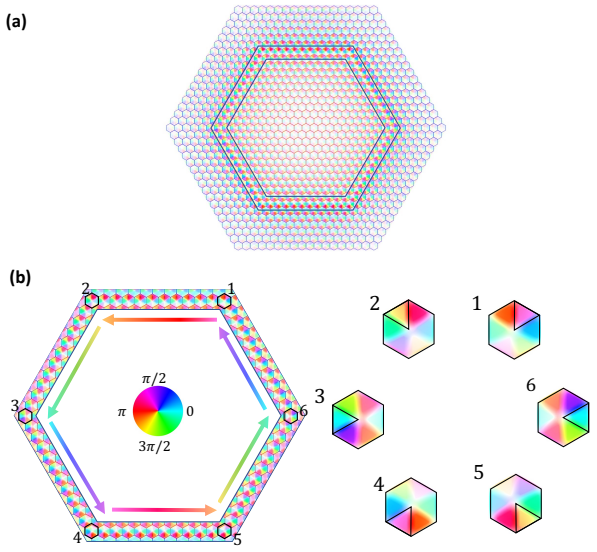

Fig. 8. (a) Phase of H_z for mode $|0,+\rangle$, where the opacity of color is proportional to $|H_z|$. (b) Distribution of the phase at the outmost layer of topological hexagonal unit cells as indicated by the hexagonal ring in (a). Six hexagons are taken to check the phase in the triangular sections. There is a 4π phase change for a rotation as indicated by the color change of arrows. The out-of-plane momentum is $k_z = 0.1 \times 2\pi/a_0$.

The same analysis can be applied to mode $|-1,+\rangle$ shown in Fig. 9(a). In this case the color changes by one loop in the counterclockwise order of the color disk when one goes a round along the azimuthal angle. This indicates a 2π change of phase corresponding to total OAM $L = 1$, and

Optics EXPRESS

$l = -1$. Phases of H_z for some other topological interface modes with pseudospin up are shown in Fig. 10.

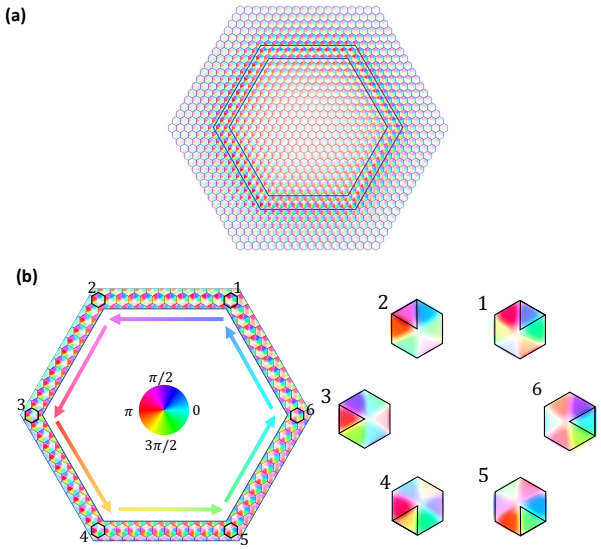

Fig. 9. (a) Phase of H_z for mode $|-1,+\rangle$, where the opacity of color is proportional to $|H_z|$. (b) Distribution of the phase at the outmost layer of topological hexagonal unit cells as indicated by the hexagonal ring in (a). Six hexagons are taken to check the phase in the triangular sections. There is a 2π phase change for a rotation as indicated by the color change of arrows. The out-of-plane momentum is $k_z = 0.1 \times 2\pi/a_0$.

Because of positive k_z, these topological interface modes have Poynting vectors $\boldsymbol{S} = \mathrm{Re}[\boldsymbol{E} \times \boldsymbol{H}^*]/2$ pointing to positive z direction. Combining with pseudospin-momentum locking effect, these modes can propogate along the fiber with a fixed rotation direction governed by pseudospin. In Fig. 11, the in-plane component of Poynting vectors averaged over individual unit cells are shown by arrows, whereas the z component is presented by color for topological interface modes. We notice that in mode $|-3,+\rangle$, which possesses negative total OAM in contrast to $|0,+\rangle$, the propagation direction of EM energy remains the same due to the pseudospin-momentum locking.

Finally, we discuss the modes inside the band gap in Fig. 7(a) where double degeneracy is lifted by the coupling Hamiltonian H_{CP} in Eqs. (8) and (9). The coupling energy is derived by [38]

$$\begin{aligned}&\int_0^\infty rdr \int_0^{2\pi} d\phi \langle l,+| \begin{bmatrix} Ck_-^2 & 0 \\ 0 & Ck_+^2 \end{bmatrix} |-l,-\rangle \\ &= \int_0^\infty rdr \int_0^{2\pi} d\phi [\mathrm{e}^{-\mathrm{i}(l+1)\phi} F(r) Ck_-^2 \mathrm{e}^{-\mathrm{i}(l+1)\phi} F(r) + \mathrm{e}^{-\mathrm{i}l\phi} F(r) Ck_+^2 \mathrm{e}^{-\mathrm{i}l\phi} F(r)].\end{aligned} \tag{18}$$

From Eq. (18), we can see that k_+ adds $\mathrm{e}^{\mathrm{i}\phi}$ while k_- adds $\mathrm{e}^{-\mathrm{i}\phi}$ to the integrand. Therefore, the first part of integration in Eq. (18) is nonzero for $l = -2$, and the second part of integration is nonzero for $l = 1$, which correspond to $L = 0$ and $L = \pm 3$ (see Fig. 7(a)).

The wavefunction of mode $|0,+\rangle$ for $k_z = 0.5 \times 2\pi/a_0$ is displayed in Fig. 12, which is almost the same as that shown in Fig. 8 for $k_z = 0.1 \times 2\pi/a_0$. Therefore, the out-of-plane momentum does not influence the mode assignment discussed above.

Optics EXPRESS

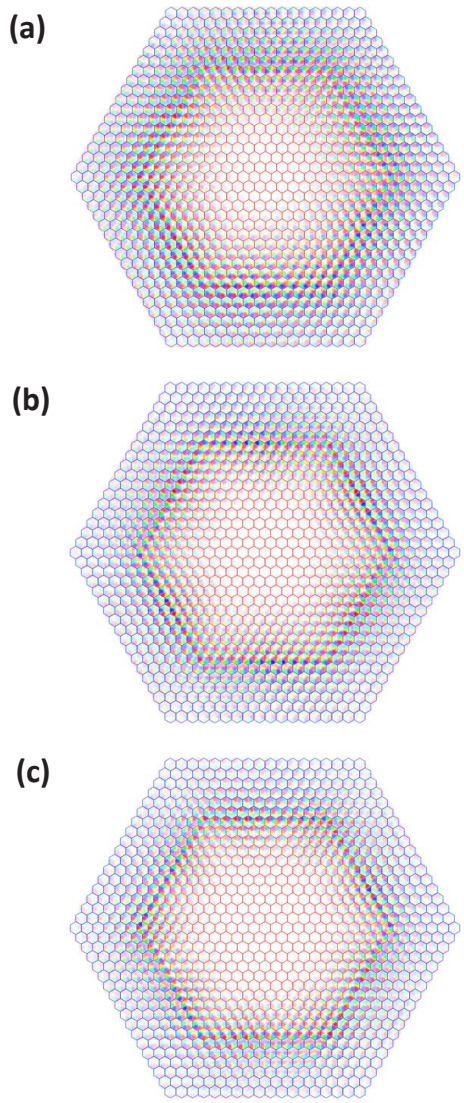

Fig. 10. (a)-(c) Phase of H_z for modes $|-3,+\rangle$, $|2,+\rangle$, $|3,+\rangle$ respectively. The out-of-plane momentum is $k_z = 0.1 \times 2\pi/a_0$.

Optics EXPRESS

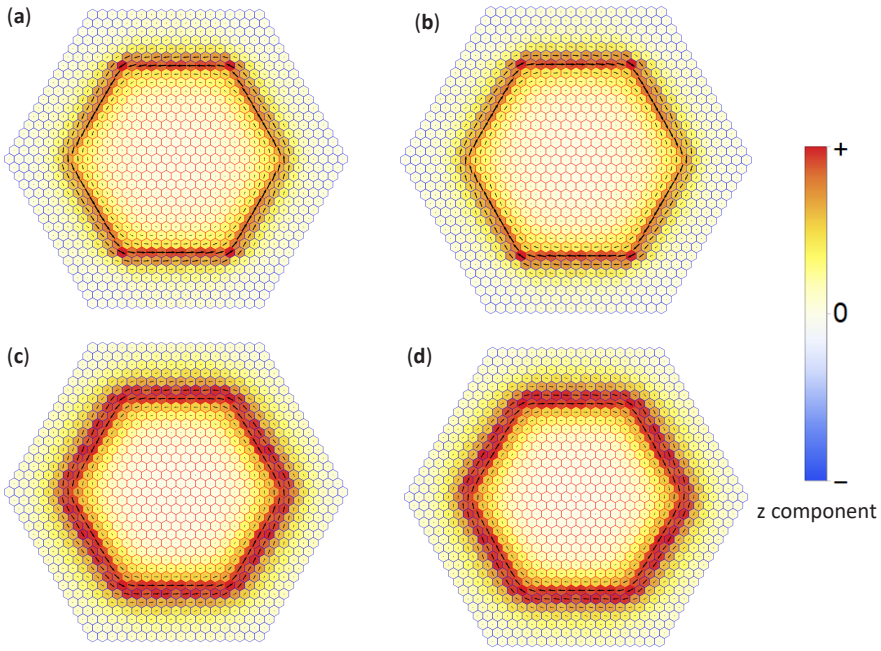

Fig. 11. (a)-(d) Poynting vectors averaged over individual unit cells for modes $|0,+\rangle$, $|0,-\rangle$, $|-3,+\rangle$ and $|3,-\rangle$ respectively, where the in-plane component is presented by arrow and the z component is shown by color. The out-of-plane momentum is $k_z = 0.1 \times 2\pi/a_0$.

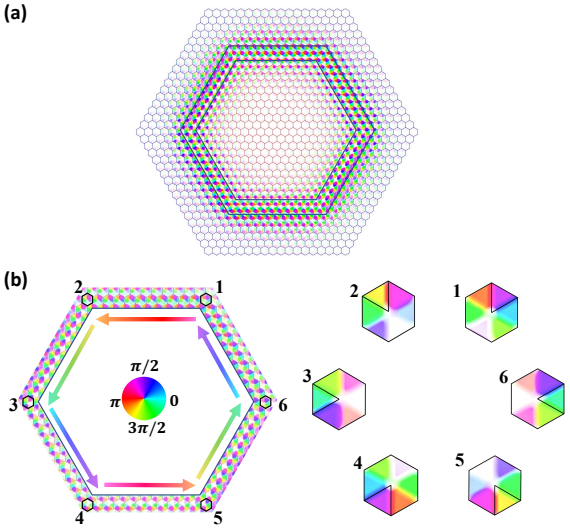

Fig. 12. (a) Phase of H_z for mode $|0,+\rangle$, where the opacity of color is proportional to $|H_z|$. (b) Distribution of the phase at the outmost layer of topological hexagonal unit cells as indicated by the hexagonal ring in (a). Six hexagons are taken to check the phase in the triangular sections. The out-of-plane momentum is $k_z = 0.5 \times 2\pi/a_0$, and the results are the same as those for $k_z = 0.1 \times 2\pi/a_0$ shown in Fig. 8.

Optics EXPRESS

4. Discussions

Refs. [27] and [28] exploit the valley-Hall effect to create the topological interfacial modes, where the Dirac-type dispersions occur at K and K' point. While the approach shares many common properties with the present one, the spin-momentum locking feature in the helical topological interfacial modes highlighted in the present work based on detailed analyses on wavefunctions were not clarified so far, which is important for understanding the polarization-to-pseudospin and vortex-to-OAM correspondence in light beams.

One can put the trivial PhC at the center and clad it by topological PhC, a dual structure to the one addressed explicitly in the present work. The psudospin-momentum locking is still available with the direction reversed, namely the pseudospin-up (-down) states exhibit clockwise (counterclockwise) energy flow.

How light can be efficiently coupled from outside to TPC fiber constitutes an interesting future problem. As demonstrated in the previous work [35], the converting efficiency between the topological interfacial mode and a silicon waveguide mode can be improved significantly by shaping the silicon waveguide in 2D PhC. Similar device structures might be developed for fiber system by tuning the shape and/or refractive index on an input conventional fiber without photonics topology. A laser based on topological interfacial modes in 2D PhC [38] can also serve as a possible input.

5. Conclusion

In the present work, we have proposed a new scheme to construct topological photonic crystal fibers where the photonics topology is induced by arrangements on the positions of air holes in hexagonal unit cells accompanied by a $p - d$ band inversion associated with the C_{6v} symmetry. While this mechanism is clear in two- dimensional systems with zero k_z, here we investigate the effect of nonzero out-of-plane k_z. The degeneracy and band inversion are also found for finite k_z, where the double degeneracy is protected by the combination of time-reversal symmetry and the mirror symmetry with respect to the cross section. In a topological photonic crystal fiber constructed by a core of topological photonic crystal surrounded by a trivial photonic crystal, topological interface modes with out-of-plane propagation are realized inside the band gap specified by the speudospin defined by the local orbital angular momentum inside the unit cell and the total orbital angular momentum with respect to the center of fiber. The topological helical interface modes with up or down pseudospin transport energy along the fiber direction in the counterclockwise or clockwise way respectively, manifesting the pseudospin-momentum locking as the characteristic feature of Z_2 topology.

Funding. Core Research for Evolutional Science and Technology (JPMJCR18T4).

Disclosures. The authors declare no conflicts of interest.

Data availability. Data underlying the results presented in this paper are not publicly available at this time but may be obtained from the authors upon reasonable request.

References

1. M. Arumugam, "Optical fiber communication—an overview," Pramana **57**(5-6), 849–869 (2001).
2. P. Sharma, R. K. Arora, S. Pardeshi, and M. Singh, "Fibre optic communications: An overview," International Journal of Emerging Technology and Advanced Engineering **3**, 474–479 (2013).
3. F. Q. Kareem, S. Zeebaree, H. I. Dino, M. Sadeeq, Z. N. Rashid, D. A. Hasan, and K. H. Sharif, "A survey of optical fiber communications: challenges and processing time influences," AJRCoS **7**, 48–58 (2021).
4. H. Kubota and T. Morioka, "Few-mode optical fiber for mode-division multiplexing," Opt. Fiber Technol. **17**(5), 490–494 (2011).
5. K. Kitayama and N.-P. Diamantopoulos, "Few-mode optical fibers: Original motivation and recent progress," IEEE Commun. Mag. **55**(8), 163–169 (2017).
6. K. Grattan and T. Sun, "Fiber optic sensor technology: an overview," Sens. Actuators, A **82**(1-3), 40–61 (2000).
7. B. Lee, "Review of the present status of optical fiber sensors," Opt. Fiber Technol. **9**(2), 57–79 (2003).

Optics EXPRESS

8. M. E. Fermann and I. Hartl, "Ultrafast fiber laser technology," IEEE J. Sel. Top. Quantum Electron. **15**(1), 191–206 (2009).
9. P. D. Dragic, M. Cavillon, and J. Ballato, "Materials for optical fiber lasers: A review," Appl. Phys. Rev. **5**(4), 041301 (2018).
10. R. Cregan, B. Mangan, J. Knight, T. Birks, P. S. J. Russell, P. Roberts, and D. Allan, "Single-mode photonic band gap guidance of light in air," Science **285**(5433), 1537–1539 (1999).
11. P. Russell, "Photonic crystal fibers," Science **299**(5605), 358–362 (2003).
12. S. A. Cerqueira, "Recent progress and novel applications of photonic crystal fibers," Rep. Prog. Phys. **73**(2), 024401 (2010).
13. C. Markos, J. C. Travers, A. Abdolvand, B. J. Eggleton, and O. Bang, "Hybrid photonic-crystal fiber," Rev. Mod. Phys. **89**(4), 045003 (2017).
14. M. Z. Hasan and C. L. Kane, "Colloquium: Topological insulators," Rev. Mod. Phys. **82**(4), 3045–3067 (2010).
15. X.-L. Qi and S.-C. Zhang, "Topological insulators and superconductors," Rev. Mod. Phys. **83**(4), 1057–1110 (2011).
16. D. Xiao, M.-C. Chang, and Q. Niu, "Berry phase effects on electronic properties," Rev. Mod. Phys. **82**(3), 1959–2007 (2010).
17. H. Weng, R. Yu, X. Hu, X. Dai, and Z. Fang, "Quantum anomalous hall effect and related topological electronic states," Adv. Phys. **64**(3), 227–282 (2015).
18. F. D. M. Haldane and S. Raghu, "Possible realization of directional optical waveguides in photonic crystals with broken time-reversal symmetry," Phys. Rev. Lett. **100**(1), 013904 (2008).
19. S. Raghu and F. D. M. Haldane, "Analogs of quantum-hall-effect edge states in photonic crystals," Phys. Rev. A **78**(3), 033834 (2008).
20. T. Ozawa, H. M. Price, A. Amo, N. Goldman, M. Hafezi, L. Lu, M. C. Rechtsman, D. Schuster, J. Simon, O. Zilberberg, and I. Carusotto, "Topological photonics," Rev. Mod. Phys. **91**(1), 015006 (2019).
21. A. B. Khanikaev and G. Shvets, "Two-dimensional topological photonics," Nat. Photonics **11**(12), 763–773 (2017).
22. L.-H. Wu and X. Hu, "Scheme for achieving a topological photonic crystal by using dielectric material," Phys. Rev. Lett. **114**(22), 223901 (2015).
23. L. Lu, H. Gao, and Z. Wang, "Topological one-way fiber of second chern number," Nat. Commun. **9**(1), 5384 (2018).
24. L. Pilozzi, D. Leykam, Z. Chen, and C. Conti, "Topological photonic crystal fibers and ring resonators," Opt. Lett. **45**(6), 1415–1418 (2020).
25. N. Roberts, G. Baardink, J. Nunn, P. J. Mosley, and A. Souslov, "Topological supermodes in photonic crystal fiber," Sci. Adv. **8**(51), eadd3522 (2022).
26. T. Ma and G. Shvets, "All-si valley-hall photonic topological insulator," New J. Phys. **18**(2), 025012 (2016).
27. M. Makwana, R. Wiltshaw, S. Guenneau, and R. Craster, "Hybrid topological guiding mechanisms for photonic crystal fibers," Opt. Express **28**(21), 30871–30888 (2020).
28. Z. Zhang, J. Lu, T. Liu, J. Gan, X. Heng, M. Wu, F. Li, and Z. Yang, "Azimuthally and radially polarized orbital angular momentum modes in valley topological photonic crystal fiber," Nanophotonics **10**(16), 4067–4074 (2021).
29. M. B. de Paz, M. G. Vergniory, D. Bercioux, A. García-Etxarri, and B. Bradlyn, "Engineering fragile topology in photonic crystals: Topological quantum chemistry of light," Phys. Rev. Res. **1**(3), 032005 (2019).
30. S. J. Palmer and V. Giannini, "Berry bands and pseudo-spin of topological photonic phases," Phys. Rev. Res. **3**(2), L022013 (2021).
31. Y. Yang, Y.-F. Xu, T. Xu, H.-X. Wang, J.-H. Jiang, X. Hu, and Z.-H. Hang, "Visualization of a unidirectional electromagnetic waveguide using topological photonic crystals made of dielectric materials," Phys. Rev. Lett. **120**(21), 217401 (2018).
32. S. Barik, H. Miyake, W. DeGottardi, E. Waks, and M. Hafezi, "Two-dimensionally confined topological edge states in photonic crystals," New J. Phys. **18**(11), 113013 (2016).
33. S. Barik, A. Karasahin, C. Flower, T. Cai, H. Miyake, W. DeGottardi, M. Hafezi, and E. Waks, "A topological quantum optics interface," Science **359**(6376), 666–668 (2018).
34. Z.-K. Shao, H.-Z. Chen, S. Wang, X.-R. Mao, Z.-Q. Yang, S.-L. Wang, X.-X. Wang, X. Hu, and R.-M. Ma, "A high-performance topological bulk laser based on band-inversion-induced reflection," Nat. Nanotechnol. **15**(1), 67–72 (2020).
35. H. Kagami, T. Amemiya, S. Okada, N. Nishiyama, and X. Hu, "Topological converter for high-efficiency coupling between si wire waveguide and topological si waveguide," Opt. Express **28**(22), 33619 (2020).
36. J. D. Jackson, *Classical electrodynamics*, 3rd ed (Wiley, New York, NY, 1999).
37. A. B. Comsol, *COMSOL Multiphysics® v.5.6*, Stockholm, Sweden.
38. X.-C. Sun and X. Hu, "Topological ring-cavity laser formed by honeycomb photonic crystals," Phys. Rev. B **103**(24), 245305 (2021).
39. G. Siroki, P. A. Huidobro, and V. Giannini, "Topological photonics: From crystals to particles," Phys. Rev. B **96**(4), 041408 (2017).
40. L.-H. Wu and X. Hu, "Topological properties of electrons in honeycomb lattice with detuned hopping energy," Sci. Rep. **6**(1), 24347 (2016).
41. T. Kariyado and X. Hu, "Topological states characterized by mirror winding numbers in graphene with bond modulation," Sci. Rep. **7**(1), 16515 (2017).
42. R. Jackiw and C. Rebbi, "Solitons with fermion number," Phys. Rev. D **13**(12), 3398–3409 (1976).